Met. Mater. Int., Vol. 23, No. 1 (2017), pp. 43~53
doi: 10.1007/s12540-017-6328-2

Interpretation of High-Temperature Tensile Properties by Thermodynamically Calculated Equilibrium Phase Diagrams of Heat-Resistant Austenitic Cast Steels

Seungmun Jung[1], Seok Su Sohn[1], Won-Mi Choi[1], Byeong-Joo Lee[1], Yong-Jun Oh[2], Seongsik Jang[3], and Sunghak Lee[1,*]

[1]Center for Advanced Aerospace Materials, Pohang University of Science and Technology, Pohang 37673, Republic of Korea
[2]Department of Advanced Materials Engineering, Hanbat National University, Daejeon 34158, Republic of Korea
[3]Research and Development Center, Key Yang Precision, Gimcheon 39542, Republic of Korea

(received date: 11 May 2016 / accepted date: 24 July 2016)

High-temperature tensile properties of three heat-resistant austenitic cast steels fabricated by varying W, Mo, and Al contents were interpreted by thermodynamically calculated equilibrium phase diagrams of austenite, ferrite, and carbides as well as microstructural analyses. A two-step calculation method was adopted to cast steel microstructures below the liquid dissolution temperature because the casting route was not an equilibrium state. Thermodynamically calculated fractions of equilibrium phases were well matched with experimentally measured fractions. Ferrites existed at room and high temperatures in both equilibrium phase diagrams and actual microstructures, which has not been reported in previous researches on austenitic cast steels. In the W2Mo1Al1 steel, 38% and 12% of ferrite existed in the equilibrium phase diagram and actual microstructure, respectively, and led to the void initiation and coalescence at ferrites and consequently to the serious deterioration of high-temperature strengths. The present equilibrium phase diagrams, besides detailed microstructural analyses, effectively evaluated the high-temperature performance by estimating high-temperature equilibrium phases, and provided an important idea on whether ferrite were formed or not in the heat-resistant austenitic cast steels.

Keywords: heat-resistant austenitic cast steel, high-temperature tensile properties, phase diagram, microstructure, strength

1. INTRODUCTION

Many researches on how to effectively control the global warming and to reduce greenhouse gases have been conducted all over the world [1-6]. In particular, the improvement of automotive engine has been focused to increase fuel efficiency and to decrease CO_2 emission, which can take economic advantages of eco-friendliness in automotive research areas [7-14]. In addition to this need of improved engine performance, automotive parts such as turbo-chargers and exhaust systems also require excellent high-temperature properties to maintain their structures at very high exhaust gas temperatures up to 950 °C, and thus heat-resistant steels such as high-temperature austenitic cast steels have been actively developed [15-19].

Highly alloyed austenitic cast steels have excellent high-temperature properties [15-21]. In recent years, they have been applied to heat-resistant automotive turbo-chargers for several inherent advantages over conventional stainless steels, such as excellent hardness, strength, fracture toughness, thermal fatigue life, and fine and stable microstructure. Their cast parts retain their shape for a prolonged time offering a good opportunity for producing high-quality cast parts for high-temperature operation. They usually contain nickel for the stabilization of austenite matrix, chromium for reduced oxidation and corrosion and increased hardness, and tungsten and niobium for carbide formation and red hardness [22-27]. Sometimes molybdenum is added for improving high-temperature hardness and for strengthening the austenite matrix [27-29].

These austenitic cast steels have different microstructures and characteristics from conventionally processed austenitic steels. When manufacturing conventional steels, the solidified ingot or slab structure is destroyed by the subsequent deformation such as hot rolling or forging after long-time homogenization, and the final microstructure consists of austenite containing fine and well-distributed carbides [30,31]. In the case of the austenitic cast steels, the cast structure containing coarse carbides in the austenite matrix is used for

*Corresponding author: shlee@postech.ac.kr

final products. Properties of austenitic cast steels are critically dependent upon the type and hardness of carbides formed during solidification. It has been reported that most of carbides are distributed mainly along solidification cell boundaries even in the finished final product [25,32], which may result in low fracture toughness and thermal fatigue property. Thus, the advantages offered by austenitic cast steels for high-quality high-temperature automotive part design may be attained by a considerable understanding of the microstructural evolution and its effect on mechanical properties, especially on high-temperature mechanical properties.

In this study, attempts are made to identify the correlation between microstructures and mechanical properties of heat-resistant austenitic cast steels. It also intends to present essential conditions in alloy designing and manufacturing by investigating effects of alloying elements. Three cast steels were fabricated by varying contents of W, Mo, and Al, and their respective effects on room- and high-temperature tensile properties were investigated. The steels were designed in such a way that the formation of homogeneously distributed hard carbides was maximized by adjusting the content of carbide formers to enhance high-temperature tensile properties. Intensive investigation was conducted on various kinds of phases existing at high temperatures, *i.e*., austenite, ferrite, and carbides, to analyze the correlation between microstructural factors and mechanical properties. In addition to the experimental approach, fractions of phases were verified by thermodynamic calculations, and the quantitative data were compared with experimentally obtained data to effectively evaluate the high-temperature performance heat-resistant austenitic cast steels.

2. EXPERIMENTAL PROCEDURE

2.1. Heat-resistant austenitic cast steels

Three austenitic steel ingots were produced in a Y-block shape (width: 50 mm, height: 110 mm, length: 180 mm) by a conventional sand casting route at Castec Korea, Busan, Korea, and their chemical compositions are shown in Table 1. These as-cast ingots were used for the present experiments after checking the homogeneity of internal and external cast structures. The 'W2Mo1' steel has a basic composition of (0.4~0.5)C-(1.2~1.5)Si-(1.1~1.3)Mn-(9.5~10.5)Ni-(20.0~22.0)Cr (wt%), along with about 4.5 wt% of strong carbide formers such as W, Nb, and Mo. 1 wt% of Al is added into the W2Mo1 steel to fabricate the 'W2Mo1Al1' steel in order to investigate the Al adding effect. Al, as a very cheap alloying element, suppresses the formation of carbides along solidification cell boundaries by reducing the C activity, and improves the overall distribution of carbides [33]. In the 'W0.5Mo2' steel, a considerable amount of W is replaced by Mo, while the W equivalent (W_{eq} = W + 2Mo) is similarly maintained. Mo has a strengthening effect of the matrix of the cast structure, and is cheaper than W [34,35]. The samples were obtained from the interior part of the as-cast ingots.

2.2. Microstructural analysis

The steel specimens were polished and etched in a 10% HCl solution (10 ml HCl + 90 ml ethanol), and microstructures were observed by an optical microscope and a scanning electron microscope (SEM, model; S-4300E, Hitach, Tokyo, Japan). Phases present in the steels were identified by X-ray diffraction (XRD, Cu Kα radiation, scan rate; 2 deg min^{-1}, scan step size; 0.02 deg) and electron probe micro analysis (EPMA, model; JXA 8530F microprobe, JEOL, Japan) employing wavelength-dispersive spectrometry (WDS) at an electron beam voltage of 15 keV. Their volume fractions were measured by an image analyzer (model; SigmaScan Pro ver. 4.0, Jandel Scientific Co., Erkrath, Germany). Electron back-scatter diffraction (EBSD) analysis (step size; 0.1 μm) was conducted by a field emission scanning electron microscope (FE-SEM, model; Quanta 3D FEG, FEI Company, USA), and the data were interpreted by an orientation imaging microscopy (OIM) analysis software provided by TexSEM Laboratories, Inc.

2.3. Room- and high-temperature tensile tests

Round tensile specimens (gage diameter; 6 mm, gage length; 25 mm) were prepared, and were tested 3 times at least for each condition at room temperature and 900 °C at a cross-head speed of 1.5 mm/min by a universal testing machine (model; 8801, Instron, Canton, MA, USA) of 100 kN capacity. A high-temperature chamber (size; 34 cm diameter × 19 cm height) was attached into the testing machine in the case of the high-temperature tensile test. The 0.2% offset stress was determined to be the yield strength. The cross-sectional areas beneath the fracture surface were observed by SEM to observe the fracture behavior.

3. RESULTS

3.1. Interpretation of high-temperature equilibrium phases by thermodynamic calculation

In the present austenitic cast steels, fractions of equilibrium

Table 1. Chemical compositions of the three austenitic cast steels (wt%)

Steel	C	Si	Mn	P	S	Ni	Cr	Nb	W	Mo	Al	W_{eq}*
W2Mo1	0.50	1.27	1.11	0.03	0.09	9.99	21.68	1.44	1.78	1.12	-	4.02
W2Mo1Al1	0.46	1.21	1.14	0.03	0.10	9.57	20.78	1.36	1.85	1.04	1.01	3.93
W0.5Mo2	0.46	1.31	1.14	0.03	0.09	9.80	21.81	1.48	0.59	2.02	-	4.63

*W_{eq} = W+2Mo (wt%)

phases existing at high temperatures were verified by thermodynamic calculations. The ThermoCalc [36], which is a commercial thermodynamic calculating program, was used for the calculation, and the upgraded version of TCFE2000 [37,38] was used for the thermodynamic database. Fractions of equilibrium phases such as liquid, austenite, ferrite, MC carbide, M_7C_3 carbide, and cementite in the temperature range of 400 °C~1400 °C are shown in Figs. 1(a) through (c). Cementite is not actually present because most of phase transformations are completed at the higher temperatures in the casting process, and thus are not considered in the calculations, although they exist below 500 °C.

In the W2Mo1 steel, the austenite, ferrite, and MC carbide start to form almost simultaneously from the liquid at 1330 ~1340 °C, and their fractions continuously increase as the fraction of liquid decreases with decreasing temperature down to 1240 °C (Fig. 1(a)). Here in the present case of cast microstructures, the rest of liquid is retained at inter-dendritic regions, and then M_7C_3 carbides are formed by reactions between three solid phases (austenite, ferrite, and MC carbide) and residual liquid phase. However, the equilibrium phase diagram of Fig. 1(a) is not basically applicable to phase analyses of cast microstructures, in which the rapid cooling rate and dendritic solidification should be preferentially considered. This is because the complete diffusion is not possible in the solid phases due to the rapid cooling, whereas it can be possibly assumed in the liquid phase [39]. Thus, the assumption that any diffusion or mixing does not occur in the solid phases during the non-equilibrium solidification process is needed. For example, the solid phases existed at 1200 °C are assumed to be homogeneous in the equilibrium state, like in Fig. 1(a), but phase fractions in the solidified microstructure cannot be defined by the equilibrium phase diagram. This is attributed to the existence of the liquid in which C is segregated at inter-dendritic regions by the solid/liquid partitioning. Below the temperature of liquid dissolution, accordingly, thermodynamic calculations of solid phases formed from the C-segregated liquid should be performed again.

The blue dotted circle is marked in Fig. 1(a), which indicated the fraction of residual liquid ($f_{L\_residue}$) at the inter-dendritic region, from which fractions of equilibrium phases are thermodynamically calculated again, as shown in Fig. 1(d). At 1250 °C, the austenite, ferrite, and M_7C_3 carbide start to form simultaneously, and the liquid is completely consumed at 1200 °C. The phase fraction of MC carbide was also calculated in Fig. 1(d), but was very low below 0.01%. Since this very low fraction is almost negligible in the total fraction of MC carbide, it does not appear in Fig. 1(d). Thus, phases formed right before the liquid dissolution (right side of the temperature of $f_{L\_residue}$ in Fig. 1(a)) exist inside solidification cells,

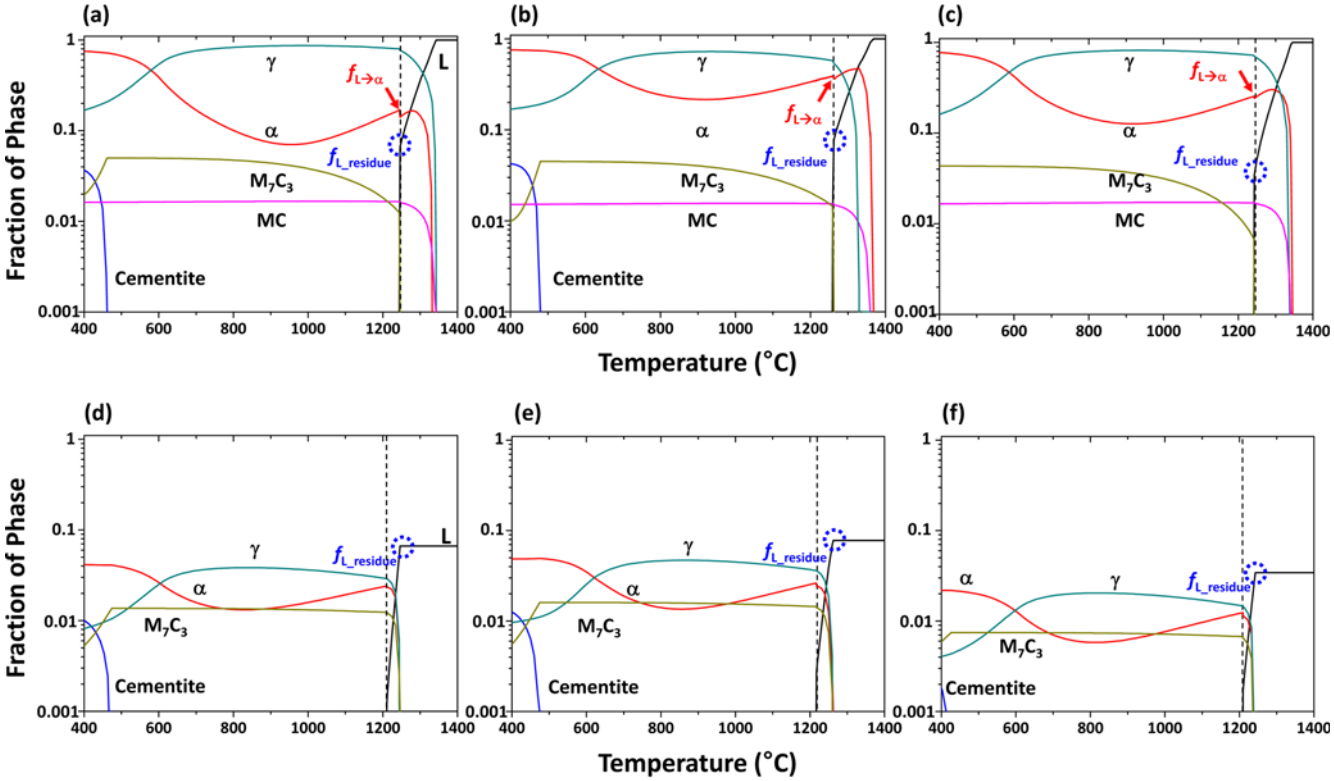

Fig. 1. Fractions of high-temperature equilibrium phases calculated by using ThermoCalc [36] for the (a) and (d) W2Mo1, (b) and (e) W2Mo1Al1, and (c) and (f) W0.5Mo2 steels. The fractions of residual liquid at inter-dendritic region are marked by blue-dotted circles in (a) through (c), from which fractions of equilibrium phases are thermodynamically calculated again, as shown in (d) through (f).

and phases formed after the liquid dissolution (left side of the temperature of $f_{L\_residue}$ in Fig. 1(d)) exist along cell boundaries. By using this two-step calculation method, fractions of equilibrium phases of the W2Mo1Al1 and W0.5Mo2 steels are obtained, as shown in Figs. 1(b) and (e) and Figs. 1(c) and (f), respectively.

The overall tendency of phase formation in the W2Mo1Al1 steel is almost same to that of the W2Mo1 steel (Figs. 1(b) and (e)). The ferrite and MC carbide start to form at 1360 °C from the liquid, while the austenite forms at 1330 °C, and the fraction of ferrite before the liquid dissolution ($f_{L\rightarrow a}$) is higher in the W2Mo1Al1 steel than in the W2Mo1 steel (a red arrow mark in Fig. 1(b)). The phase formation behavior of the W0.5Mo2 steel is similar to that of the W2Mo1 steel, although the ferrite fraction is slightly higher in the W0.5Mo2 steel (a red arrow mark in Fig. 1(c)). Assuming that, because of rapid cooling during casting, the diffusion between solid phases does not occur after the formation of solid phases, fractions of phases formed from the liquid (fractions at black-dotted lines of Figs. 1(a) through (c)) and the residual liquid (fractions at black-dotted lines of Figs. 1(d) through (f)) are shown in Table 2. In the W2Mo1 steel, for example, fractions of austenite, ferrite, MC carbide, and M_7C_3 carbide at the black-dotted line of Fig. 1(a) are combined with fractions of austenite, ferrite, and M_7C_3 carbide at the black-dotted line of Fig. 1(d), which are the total fractions of equilibrium phases. The fractions of ferrite and total carbide are much higher in the W2Mo1Al1 steel than in the other steels. The fraction of total carbide is lowest in the W2Mo1 steel.

3.2. Microstructure

Figures 2(a) through (c) are optical micrographs of the as-cast W2Mo1, W2Mo1Al1, and W0.5Mo2 steels. A considerable number of carbides are located mostly along boundaries of solidification cells, whose sizes are similar (60~70 μm) in the three steels. The X-ray diffraction analysis was conducted on the steels, and the results are shown in Figs. 3(a) through (c). In all the steels, peaks of MC- and M_7C_3-type carbides as well as austenite are observed, while peaks of ferrite are additionally found in the W2Mo1Al1 steel, as indicated by blue square symbols in Fig. 3(b). Since MC- and M_7C_3-type carbides are mixed together along solidification cell boundaries (Figs. 2(a) through (c)), they are identified by SEM micrograph and EPMA mapping analysis data of the W2Mo1Al1 steel, as shown in Fig. 4. MC carbides are Nb-rich carbides containing mostly Nb with small amounts of W, Mo, Cr, and Fe [40]. Thus, white-colored Nb-rich region and gray-colored Cr-rich coral-shape region indicate MC- and M_7C_3-type carbides, respectively. The hardness of MC carbide (2740 VHN) is higher than that of M_7C_3 carbide (2380 VHN respectively) [41] as well as austenite matrix (210 VHN). From the detailed microstructural analyses coupled with EPMA mapping, MC and M_7C_3 carbides, austenite, and ferrite are marked by arrows in Figs. 2(a) through (c).

Table 3 lists the quantitative analysis results of solidification cell size and volume fractions of austenite, ferrite, and carbide. Solidification cells in the W2Mo1, W2Mo1Al1, and W0.5Mo2 steels are sized by 65 μm, 59 μm, and 71 μm, respectively, which shows similar sizes within small standard deviations. Volume fractions of MC and M_7C_3 carbides in the W2Mo1 steel are 1.9% and 3.0%, respectively, and M_7C_3 carbides are more populated. In the W2Mo1Al1 steel, the volume fraction of total carbides is slightly higher than in the W2Mo1 steel as many M_7C_3 carbides are formed. The W0.5Mo2 steel contains the lowest volume fraction of M_7C_3 carbides, and thus shows the lowest volume fraction of total carbides. These results of car-

Table 2. Thermodynamically calculated fractions of austenite, ferrite, and carbides in the austenitic cast steels (unit: %)

Steel	Austenite	Ferrite	MC Carbide	M_7C_3 Carbide	Total Carbide
W2Mo1	Bal.	15.6	1.65	2.50	4.15
W2Mo1Al1	Bal.	38.0	1.50	2.95	4.45
W0.5Mo2	Bal.	24.7	1.70	1.40	3.10

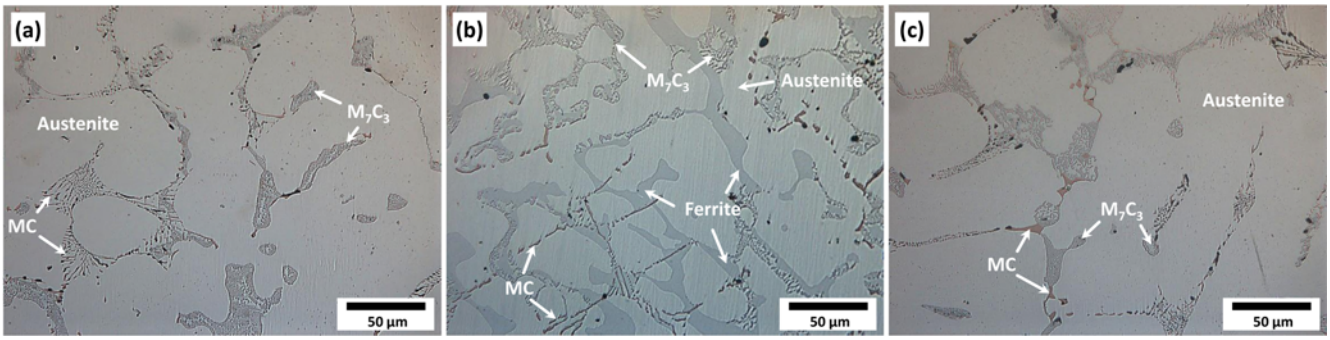

Fig. 2. Optical micrographs of the (a) W2Mo1, (b) W2Mo1Al1, and (c) W0.5Mo2 steels, showing relatively coarse carbides in the austenite matrix. Etched in a 10% HCl solution.

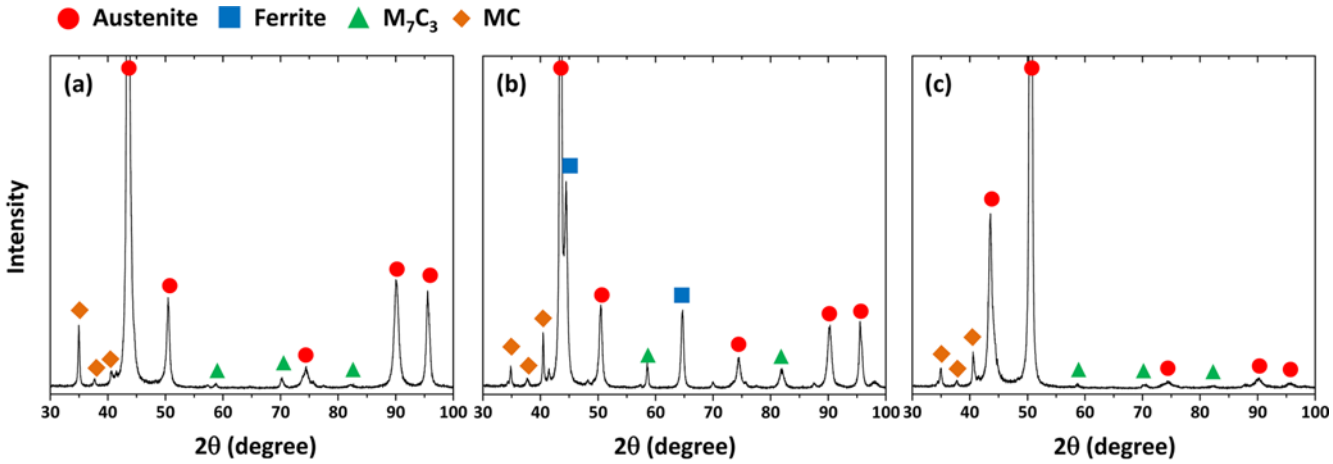

Fig. 3. X-ray diffraction analysis data of the (a) W2Mo1, (b) W2Mo1Al1, and (c) W0.5Mo2 steels. In all the three steels, peaks of MC- and M_7C_3-type carbides as well as austenite are observed, while peaks of ferrite are additionally found in the W2Mo1Al1 steel.

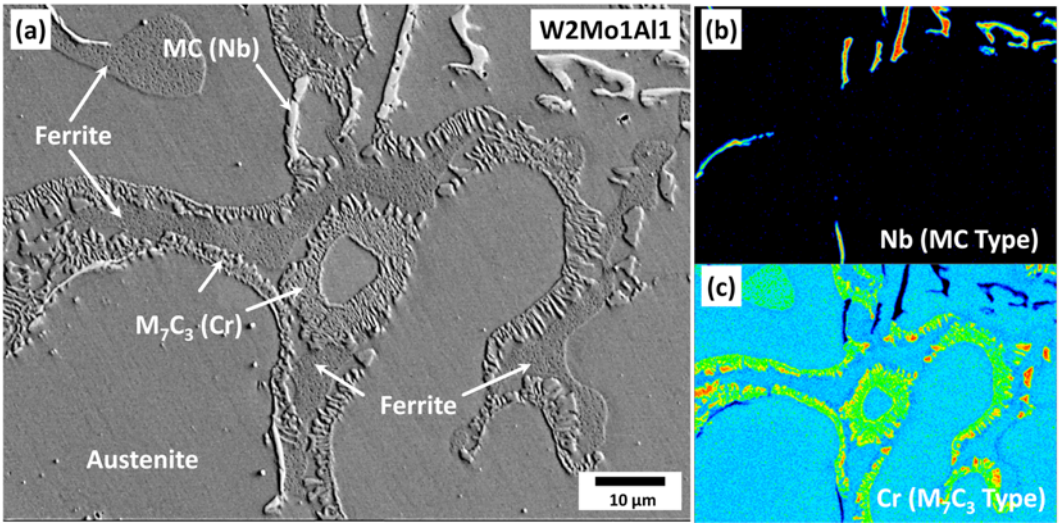

Fig. 4. (a) SEM micrograph, and (b) and (c) EPMA mapping analysis data of W2Mo1Al1 steel, showing (b) MC- and (c) M_7C_3-type carbides as indicated by arrows.

Table 3. Quantitative analysis results of solidification cell size and volume fractions of austenite, ferrite, and carbides measured by an image analyzer in the austenitic cast steels at room temperature (unit: %)

Steel	Cell Size (μm)	Austenite	Ferrite	MC Carbide	M_7C_3 Carbide	Total Carbide
W2Mo1	65 ± 2.0	Bal.	-	1.9 ± 0.5	3.0 ± 0.7	4.9 ± 0.5
W2Mo1Al1	59 ± 5.4	Bal.	12.4 ± 2.7	1.5 ± 0.5	3.6 ± 0.8	5.1 ± 1.3
W0.5Mo2	71 ± 4.5	Bal.	-	2.0 ± 0.6	2.1 ± 0.7	4.1 ± 1.1

bide volume fractions are well matched with thermodynamically calculated data, although the calculated volume fractions are somewhat underestimated. About 12 vol% of ferrite is found in the W2Mo1Al1 steel, while it is not found at all in the other two steels. In order to confirm the existence of ferrite in the W2Mo1Al1 steel, an EBSD image quality phase map is shown in Fig. 5. About 12 vol% of ferrite is observed again, and its distribution is relatively homogeneous in the austenite matrix, irrespective of the existence of solidification cell boundaries.

3.3. Room- and high-temperature tensile properties

Engineering tensile stress-strain curves tested at room and high (900 °C) temperatures are shown in Figs. 6(a) and (b). From the curves, the yield strength, tensile strength, and elongation were measured, and the results are summarized in Table 4. The W2Mo1 steel has the yield strength, tensile strength, and elongation of 376 MPa, 643 MPa, and 8.8%, respectively, at room temperature. It shows a relatively high strain hardening. With adding Al content into the W2Mo1 steel, the tensile

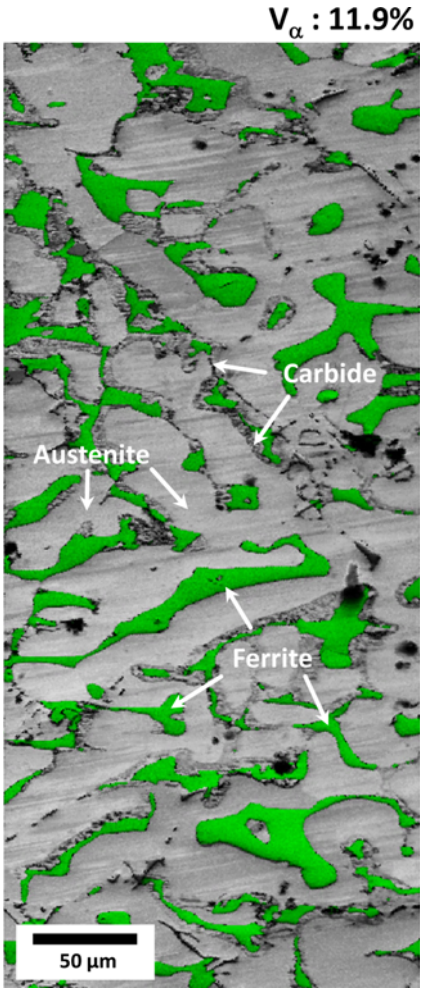

Fig. 5. EBSD image quality phase map of the W2Mo1Al1 steel, showing the formation of ferrite in an isolated shape in the austenite matrix.

strength slightly increases, and the elongation decreases, which indicates the almost same tensile deformation behavior (Fig. 6(a)). The W0.5Mo2 steel also shows the similar behavior, although overall tensile properties are lowest among the three steels. At 900 °C, the yield and tensile strengths are much lower than the room-temperature strengths, but the elongation is much higher (Figs. 6(a) and (b)). The W2Mo1 and W0.5Mo2 steels show the similar tensile deformation behavior, but the W0.5Mo2 steel has the slightly higher strengths and the lower elongation. The large reduction in strength is observed in the W2Mo1Al1 steel in comparison to the other steels, while the elongation increases. The strain hardening disappears in all the steels.

Optical micrographs of the cross-sectional area beneath the fracture surface of the room-temperature tensile specimen are shown in Figs. 7(a) through (f). The fracture occurs in the direction vertical to the tensile loading direction with almost no necking phenomenon (Figs. 7(a) through (c)). When the microstructures are magnified (Figs. 7(d) through (f)), most of fracture paths follow the intercellular region populated with carbides (along cell boundaries). A considerable number of microcracks are observable along solidification cell boundaries as marked by arrows.

Optical micrographs of the cross-sectional area beneath the fracture surface of the 900 °C tensile specimen are shown in Figs. 8(a) through (g). The fracture occurs with a considerable amount of necking (Figs. 8(a) through (c)) as the high-temperature specimens show some ductility (Fig. 6(b)). The overall microstructures composed of intercellular carbides and austenite matrix are elongated along the tensile direction (Figs. 8(d) through (f)). In the W2Mo1 and W0.5Mo2 steels, most of microcracks are found along solidification cell boundaries as indicated by arrows, along which they are connected to develop to the final fracture (Figs. 8(d) and (e)). In the W2Mo1Al1 steel, a few microcracks are observed along solidification cell boundaries, but the fracture path follows mostly through the austenite matrix mixed with ferrite (Fig. 8(f)). When the deformed interior region is observed (Fig. 8(g)), a number of voids are found in ferrite areas.

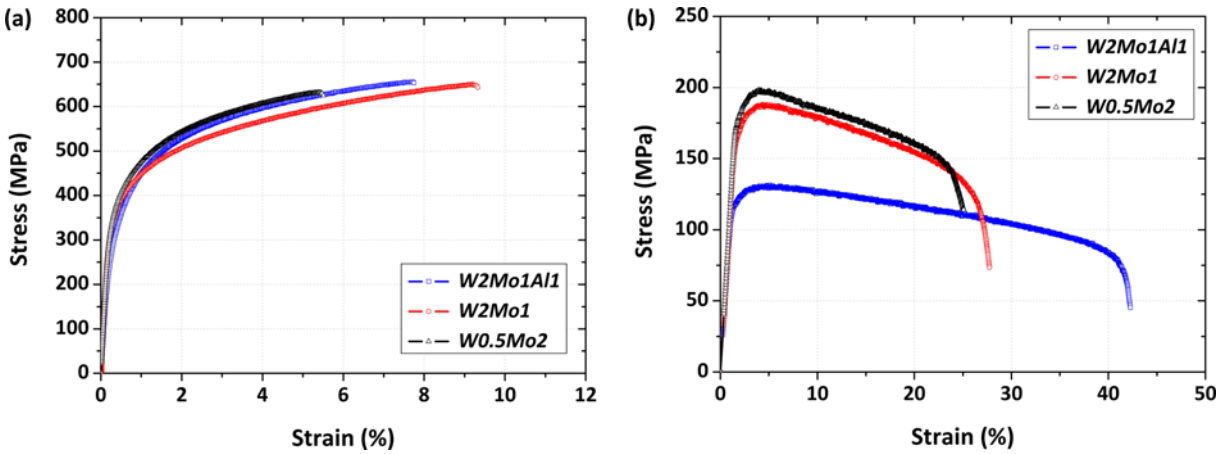

Fig. 6. Engineering stress-strain curves of the steels tested at (a) 25 °C and (b) 900 °C.

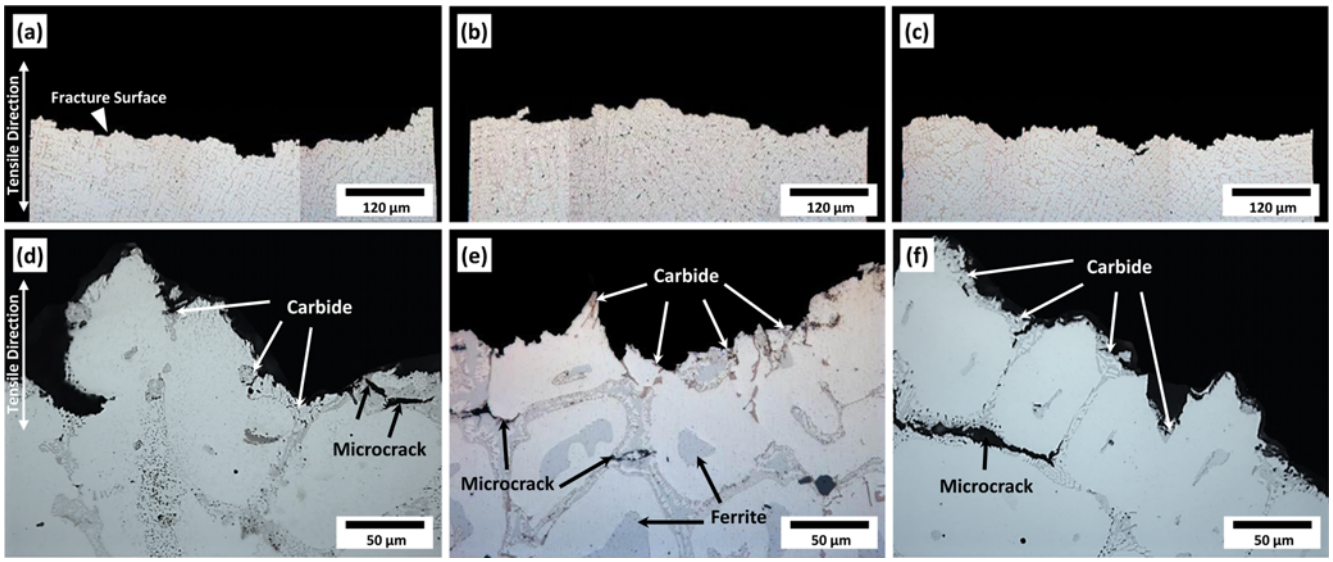

Fig. 7. Optical micrographs of the cross-sectional area beneath the fracture surface of the room-temperature tensile specimen of the (a) and (d) W2Mo1, (b) and (e) W2Mo1Al1, and (c) and (f) W0.5Mo2 steels.

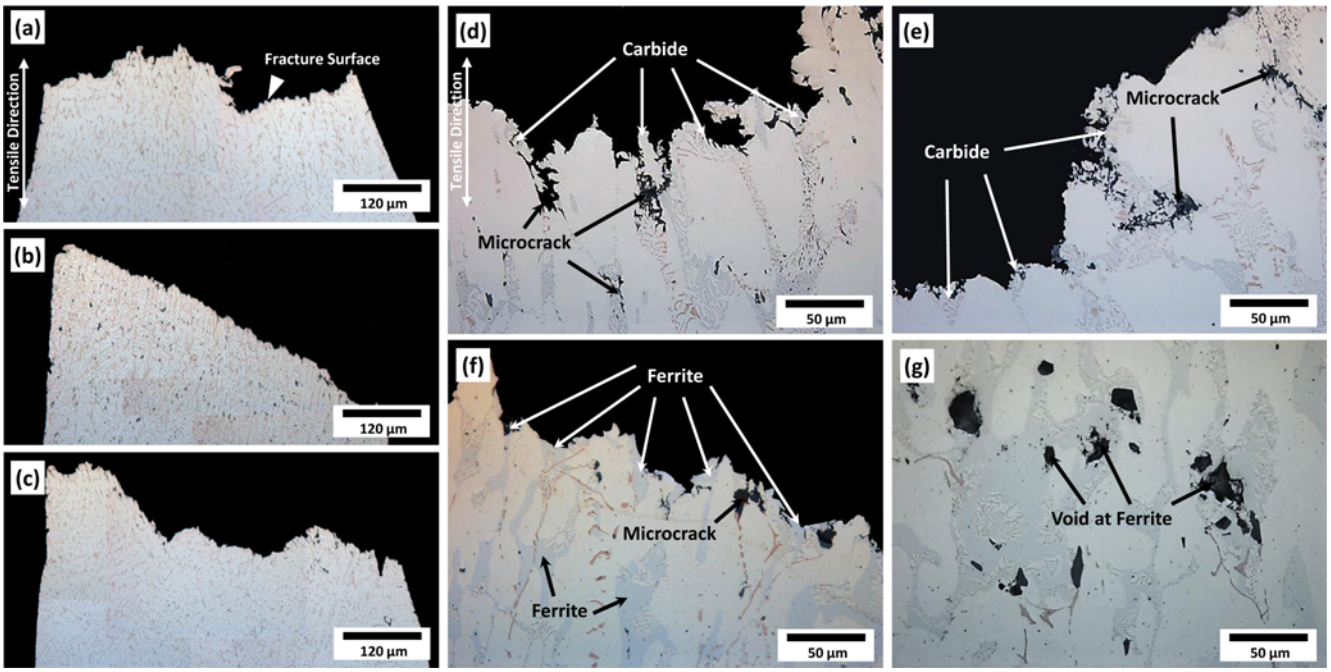

Fig. 8. Optical micrographs of the cross-sectional area beneath the fracture surface of the 900 °C tensile specimen of the (a) and (d) W2Mo1, (c) and (e) W0.5Mo2, and (b), (f), and (g) W2Mo1Al1 steels.

4. DISCUSSION

Heat-resistant austenitic cast steels are generally characterized of excellent high-temperature strengths and resistance to oxidization and thermal fatigue by adding strong carbide formers like Nb, W, Mo, and Cr to form very hard carbides of MC and M_7C_3 [40,41]. However, the austenitic cast steels currently manufactured by a conventional sand casting route retain coarse solidification cell structures and carbides formed during casting because they cannot be subjected to subsequent heavy deformation processes such as forging or rolling [42,43]. High-temperature properties of austenitic cast steels are determined by various microstructural factors such as; 1) kind, shape, volume fraction, and distribution of carbides, 2) characteristics of the austenite matrix, and 3) solidification cell structure made up of carbides. Carbides directly influence high-temperature strengths since they are very hard and stable at high temperatures. The austenite matrix is related

with overall hardness, strength, and fracture toughness, and plays a sustaining role for hard carbides. The solidification cell size also plays a role in determining the overall carbide distribution. Thus, these microstructural factors should be controlled in optimal combinations to achieve excellent high-temperature properties.

In order to analyze effects of alloying elements added to the austenitic cast steels, equilibrium phase diagrams based on thermodynamic calculations, as in Figs. 1(a) through (f), are useful [44,45]. Though these diagrams are concerned with equilibrium phases existing at high temperatures, it can be reasonably applied to the alloy compositions of the austenitic cast steels. Figures 1(a) through (f) show the variation in fractions of phases such as liquid, austenite, ferrite, and MC and M_7C_3 carbides with decreasing temperature from 1400 °C. These phases exist in the actual microstructures (Figs. 2(a) through (c)), which indicates the good correspondence between equilibrium phase diagrams and actual microstructures. It is interesting to note that the ferrite exists as an equilibrium phase in both equilibrium phase diagrams and actual microstructures, although the sufficient stability of austenite is expected by adding about 10 wt% of Ni, a potent austenite stabilizer, into the present cast steels. In the W2Mo1Al1 steel, 38% of ferrite exists at room temperature in the equilibrium phase diagram (Table 2) because Al works as a strong ferrite stabilizer, while 12 vol% of ferrite exists in the actual microstructure (Table 3). The difference in the calculated fraction and measured volume fractions of ferrite is attributed to the non-equilibrium state in the casting process. In fact, the thermodynamic calculation is based on completely equilibrium state without considering kinetic processes of phase formation, and thus the estimation of phase fraction does not completely reflect the actual microstructure [46,47]. Since the cast steels are rapidly cooled during casting, the equilibrium state cannot be retained. In the W2Mo1 and W0.5Mo2 steels, the ferrite is not found, as shown in Figs. 2(a) and (c) in Table 3, although the calculated fraction of ferrite ranges from 15% to 25% (Table 2). This implies that the ferrite exists in the actual microstructure when the fraction of ferrite is higher than 25% in the equilibrium phase diagrams.

The existence of ferrite greatly influences high-temperature mechanical properties. In the room-temperature tensile test, the tensile behavior of the ferrite-containing W2Mo1Al1 steel is similar to that of the non-ferrite-containing W2Mo1 and W0.5Mo2 steels (Fig. 6(a)). This is because room-temperature properties of ferrite are not much different from those of austenite, and because the ferrite is well distributed in an isolated shape in the austenite matrix. At high temperature, on the contrary, the ferrite can play an important role in reducing the strength. In order to investigate the existence of ferrite during the tensile test at 900 °C, the three steels were held at 900 °C for 30 min (approximately equal time to the tensile testing time) and then quenched to room temperature. Their XRD data and EBSD phase maps are shown in Figs. 9 and 10, respectively. According to the XRD data, peaks of bcc ferrite are found in the W2Mo1Al1 steel, whereas they are not in the other steels (Figs. 9(a) through (c)). The EBSD phase map of the W2Mo1Al1 steel shows the existence of ferrite at 900 °C (Figs. 10), which corresponds with the XRD data. The ferrite volume fraction is reduced from 12% to 9% as the temperature increases from room temperature to 900 °C, as expected from the equilibrium phase diagram of Fig. 1(b). Since high-temperature properties of ferrite are much worse than those of austenite [48,49], even a small amount of ferrite critically deteriorates high-temperature properties, particularly strength, of the W2Mo1Al1 steel (Table 4).

According to the microstructural analysis of the deformed region of the 900 °C tensile specimen (Figs. 8(d) through (g)), the fracture behavior of the W2Mo1Al1 steel is different from that of the other steels. In the W2Mo1 and W0.5Mo2 steels, microcracks are readily observed in carbide-populated intercellular regions (Figs. 8(d) and (e)), but the W2Mo1Al1 steel

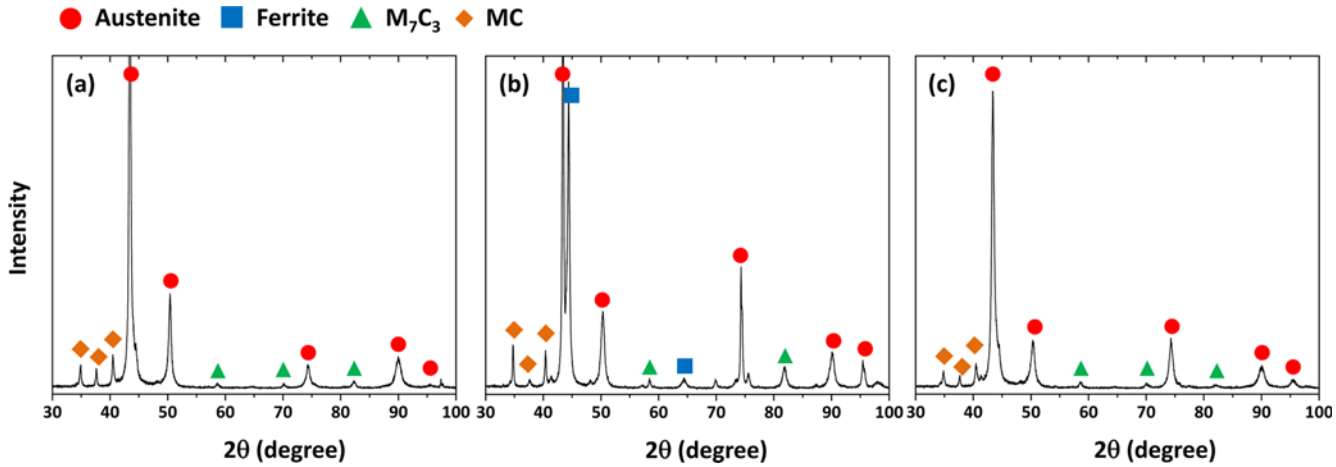

Fig. 9. X-ray diffraction analysis data of the (a) W2Mo1, (b) W2Mo1Al1, and (c) W0.5Mo2 steels quenched from 900 °C.

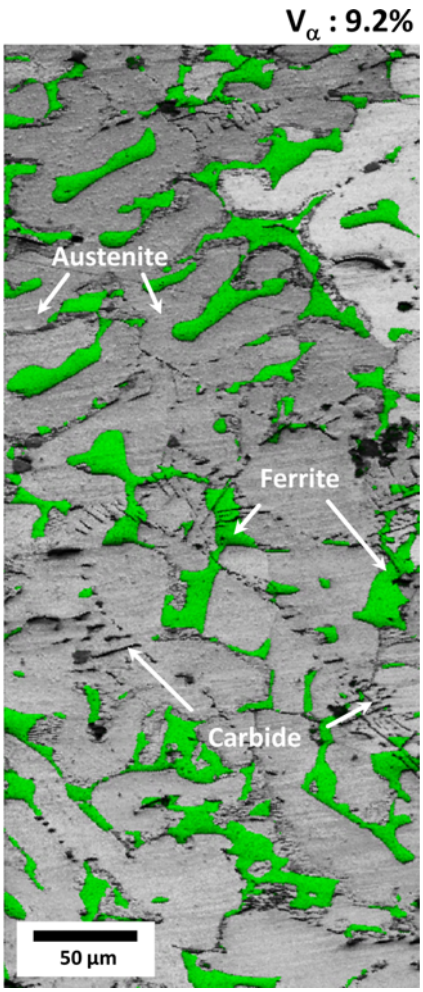

Fig. 10. EBSD image quality phase color map of the W2Mo1Al1 steel quenched from 900 °C.

is mostly fractured by the initiation of voids at ferrites and their coalescence as the ferrites are heavily elongated at 900 °C, whereas voids are hardly found in the austenite matrix (Fig. 8(g)). This easy initiation of voids in the W2Mo1Al1 steel is closely related with the deteriorated high-temperature strength of the ferrite [49], which critically reduces the strength.

The thermodynamically calculated equilibrium phase diagrams (Figs. 1(a) through (f)) also show the precipitation behavior of MC and M_7C_3 carbides, which are present in the actual microstructures (Figs. 2(a) through (c)). The fraction of MC carbide ranges from 1.5% to 1.7% in the phase diagrams (Table 2), while it ranges from 1.5% to 2.0% in the optical micrographs (Table 3), but the overall trends of fraction of MC carbide are same in the both calculated and measured data of the three steels. The fraction of M_7C_3 carbide also shows the same trend. This indicates that the calculated and measured carbide fraction data are well matched. The reason for this well-matched data in the carbide fraction, unlike in the ferrite fraction, is closely related to the fact that the variation in fraction of carbides with temperature is not large, and that the non-equilibrium state of casting is not much different from the equilibrium state in the case of carbide formation.

It is interesting that the volume fraction of total carbides is highest in the W2Mo1Al1 steel. Zuidema *et al*. [33] reported that Al improved the carbon distribution by preventing the carbide formation at solidification cell boundaries. However, they might not consider the possibility of ferrite formation due to the addition of Al. In the W2Mo1Al1 steel containing 12 vol% of ferrite whose carbon solubility is very low, the carbon concentration in the austenite considerably increases to promote the precipitation of carbides (Table 3), thereby resulting in the highest tensile strength at room temperature (Table 4). At 900 °C, the W2Mo1Al1 steel shows the lowest tensile strength because the strength-reducing effect of ferrite greatly overrides the strength-raising effect of carbides. In the W2Mo1 and W0.5Mo2 steels, room-temperature tensile properties are similar because of the absence of ferrite and the similar carbide fraction. However, high-temperature yield and tensile strengths are higher in the W0.5Mo2 steel than in the W2Mo1 steel, which is not readily explained by the difference in carbide volume fraction.

The high-temperature strength is also affected by solid-solution strengthening in the austenite matrix. In order to examine the extent of solid-solution strengthening, W and Mo contents inside the austenite matrix were analyzed by energy dispersive spectroscopy (EDS), and the results are shown in Table 5. Since the effect of W and Mo on solid-solution strengthening is proportional to atomic percentage, instead of weight percentage, Mo is twice more effective than W, as shown in tungsten equivalent (W_{eq}=W+2Mo). Considering the atomic percentage of W and Mo contained inside the austenite matrix, more solid-solution-strengthening elements are included in the W0.5Mo2 steel than in the W2Mo1 steel. Thus, the W0.5Mo2 steel shows the higher strengths at 900 °C than the W2Mo1 steel, although these two steels have similar microstructures.

Table 4. Room- and high-temperature tensile test results of the austenitic cast steels

Steel	Room Temperature			High Temperature (900 °C)		
	Yield Strength (MPa)	Tensile Strength (MPa)	Tensile Elongation (%)	Yield Strength (MPa)	Tensile Strength (MPa)	Tensile Elongation (%)
W2Mo1	376 ± 6	643 ± 10	8.8 ± 0.6	160 ± 5	187 ± 1	28.1 ± 3.1
W2Mo1Al1	346 ± 3	655 ± 5	7.3 ± 0.8	114 ± 1	130 ± 2	42.8 ± 0.7
W0.5Mo2	391 ± 9	615 ± 14	5.0 ± 1.0	174 ± 7	199 ± 13	25.4 ± 1.1

Table 5. W and Mo contents in the austenite matrix measured by energy dispersive spectroscopy (EDS) analysis of the austenitic cast steels

Steel	W		Mo	
	wt%	at%	wt%	at%
W2Mo1	1.4 ± 0.21	0.3 ± 0.05	2.2 ± 0.30	1.1 ± 0.29
W2Mo1Al1	1.7 ± 0.03	0.5 ± 0.02	2.2 ± 0.03	1.1 ± 0.01
W0.5Mo2	0.5 ± 0.11	0.1 ± 0.04	3.9 ± 0.49	2.2 ± 0.24

These investigations on effects of microstructural factors on room- and high-temperature tensile properties not only expand the understanding of the austenitic cast steels, but also provide the basic data required to enhance high-temperature tensile properties. High-temperature strengths can be improved by promoting a large amount of hard carbides and solid-solution-strengthened austenite matrix. However, there exists the ferrite as an equilibrium phases at room and high temperatures in both thermodynamic calculated equilibrium phase diagrams and actual microstructures, which has not been reported in previous researches on austenitic cast steels or stainless steels [15-21]. In the W2Mo1Al1 steel, 38% and 12% of ferrite exists at room temperature in the equilibrium phase diagram and actual microstructure, respectively, and leads to the easy void initiation and coalescence at ferrites and consequently to the serious deterioration of high-temperature strengths. The present equilibrium phase diagrams, besides detailed microstructural analyses, effectively evaluate the high-temperature performance by estimating high-temperature equilibrium phases, and provide an important idea on whether ferrites are formed or not in the heat-resistant austenitic cast steels.

5. CONCLUSIONS

In this study, room- and high-temperature tensile properties of three heat-resistant austenitic cast steels fabricated by varying W, Mo, and Al contents were interpreted by thermodynamically calculated equilibrium phase diagrams as well as detailed microstructural evolution analyses.

(1) Fractions of equilibrium phases such as austenite, ferrite, and carbides existing at high temperatures were verified by thermodynamic calculations. A two-step calculation method was adopted to the present austenitic cast steel microstructures below the liquid dissolution temperature because the casting route was not an equilibrium state. Thermodynamically calculated fractions of solid phases were well matched with experimentally measured fractions, although there were some differences between the two fractions.

(2) In the W2Mo1Al1 steel, 38% of ferrite existed at room temperature in the equilibrium phase diagram because Al worked as a strong ferrite stabilizer, while 12 vol% of ferrite existed in the actual microstructure. The difference in the calculated and measured fractions of ferrite was attributed to the non-equilibrium state in the casting process. In the W2Mo1 and W0.5Mo2 steels, the ferrite was not found in the actual microstructure, although the calculated fractions of ferrite were ranged from 15 to 25%. This implied that the ferrite was formed when the calculated fraction of ferrite was higher than 25%.

(3) At high temperature, the non-ferrite-containing W2Mo1 and W0.5Mo2 steels were fractured by the formation of microcracks in carbide-populated intercellular regions without any voids. On the other hand, the W2Mo1Al1 steel was mostly fractured by the initiation of voids at ferrites and their coalescence, whereas voids were hardly found in the austenite matrix. The existence of ferrites and easy initiation of voids at them, which have not been reported in previous researches on austenitic cast steels or stainless steels, led to the serious deterioration of high-temperature strength of the ferrite-containing steel.

ACKNOWLEDGMENTS

This work was supported by the World Class 300 Project R&D Program (10050290-2013-39) and the Future Material Discovery Program of the National Research Foundation of Korea (NRF) funded by the Ministry of Science, ICT, and Future Planning (MSIP) of Korea (2016M3D1A1023384). Authors are grateful to Mr. Gi-Yong Kim and Mr. Hyeungjun Kim of Key Yang Precision for their helpful discussion on the fabrication of heat-resistant austenitic cast steels.

REFERENCES

1. R. D. Schuiling and P. L. Boer, *Int. J. Greenh. Gas Con.* **4**, 855 (2010).
2. M. Meinshausen, N. Meinshausen, W. Hare, S. C. B. Raper, K. Frieler, R. Knutti, D. J. Frame, and M. R. Allen, *Nature* **458**, 1158 (2009).
3. D. Gielen, *Energ. Convers. Manage*. **44**, 1027 (2003).
4. D. Gielen and Y. Moriguchi, *Energ. Policy* **30**, 849 (2002).
5. T. I. So, H. C. Jung, C. D. Lee, and K. S. Shin, *Met. Mater. Int.* **21**, 842 (2015).
6. S. S. Sohn, B.-J. Lee, S. Lee, and J.-H. Kwak, *Met. Mater. Int.* **21**, 43 (2015).
7. X. Tauzia, A. Maiboom, and S. R. Shah, *Energy* **35**, 3628 (2010).
8. D. H. Lee, J. S. Park, M. R. Ryu, and J. H. Park, *Appl. Therm. Eng.* **50**, 491 (2013).
9. K. Sim, B. Koo, C. H. Kim, and T. H. Kim, *Appl. Energ.* **102**, 309 (2013).
10. H.-J. Kim, G. A. Keoleian, and S. J. Skerlos, *J. Ind. Ecol.* **15**, 64 (2011).
11. A. Tharumarajah and P. Koltun, *J. Clean. Prod.* **15**, 1007 (2007).
12. P. Leduc, B. Dubar, A. Ranini, and G. Monnier, *Oil Gas Sci. Technol.* **58**, 115 (2003).

13. D.-H. Koh, Y.-S. Lee, M.-S. Kim, H.-W. Kim, and Y.-S. Ahn, *Korean J. Met. Mater.* **54**, 483 (2016).
14. B.-R. Jin and C.-Y. Jeong, *Korean J. Met. Mater.* **54**, 626 (2016).
15. Y.-J. Kim, H. Jang, and Y.-J. Oh, *Mat. Sci. Eng. A* **526**, 244 (2009).
16. N. Nagata, K. Furuya, and R. Watanabe, *J. Nucl. Mater.* **85-86**, 839 (1979).
17. T. Seifert, C. Schweizer, M. Schlesinger, M. Moser, and M. Eibl, *Int. J. Mater. Res.* **101**, 942 (2010).
18. J. P. Shingledecker, P. J. Maziasz, N. D. Evans, and M. J. Pollard, *Int. J. Pres. Ves. Pip.* **84**, 21 (2007).
19. M. Ike, K. Akiyama, K. Ohtsuka, and K. Itoh, *Int. J. Mater. Prod. Tec.* **6**, 243 (1991).
20. X. Xu, X. Zhang, G. Chen, and Z. Lu, *Mater. Lett.* **65**, 3284 (2011).
21. P. Y. Chen, R. Lyons, M. Rakoczy, K. Otsuka, H. Yamanaka, and T. Mimata, *SAE 1996, World Congress*, Paper No. 962169, Detroit, MI (1996).
22. H. Bhadeshia and R. W. K. Honeycombe, *Steels - Microstructure and Properties*, pp.259-286, Butterworth-Heinemann, Oxford, UK (2011).
23. R. L. Klueh, *Int. Mater. Rev.* **50**, 287 (2005).
24. V. Lepingle, G. Louis, D. Allue, B. Lefebvre, and B. Vandenberghe, *Corros. Sci.* **50**, 1011 (2008).
25. Y.-J. Kim, D.-G. Lee, H. K. Jeong, Y.-T. Lee, and H. Jang, *J. Mater. Eng. Perform.* **19**, 700 (2009).
26. Z. Li, Q. Yong, Z. Zhang, X. Sun, J. Cao, H. Qi, and Z. Liao, *Met. Mater. Int.* **20**, 801 (2014).
27. S. G. Hong, W. B. Lee, and C. G. Park, *J. Nucl. Mater.* **288**, 202 (2001).
28. T. Ishitsuka and H. Mimura, *JSME Int. J. A* **45** 110 (2002).
29. Q. Han, Y. Kang, X. Zhao, L. Gao, and X. Qiu, *Int. J. Min. Met. Mater.* **18**, 407 (2011).
30. H. Zhang, K. G. Pradeep, S. Mandal, D. Ponge, and D. Raabe, *Acta Mater.* **80**, 296 (2014).
31. D. Raabe, *Acta Mater.* **45**, 1137 (1997).
32. L. H. Almeida, A. F. Ribeiro, and I. L. May, *Mater. Charact.* **49**, 219 (2003).
33. B. K. Zuidema, D. K. Subramanyam, and W. C. Leslie, *Metall. Mater. Trans. A* **18**, 1629 (1987).
34. London Metal Exchange, http://www.lme.com (accessed April 1st of 2015).
35. MetalPrices.com, http://www.metalprices.com (accessd April 1, 2015).
36. B. Sundman, B. Jansson, and J.-O. Andersson, *CALPHAD* **9**, 153 (1985).
37. TCFE2000, *The Thermo-Calc Steels Database*, upgraded by B.-J. Lee and B. Sundman at KTH, Stockholm, Sweden (1999).
38. B.-J. Lee, Pohang University of Science and Technology (POSTECH), Korea, unpublished update of thermodynamic database.
39. D. Eskin, Q. Du, D. Ruvalcaba, and L. Katgerman, *Mat. Sci. Eng. A* **405**, 1 (2005).
40. W. B. Lee, S. G. Hong, C. G. Park, and S. H. Park, *Metall. Mater. Trans. A* **33**, 1689 (2002).
41. K. C. Hwang, S. Lee, and H. C. Lee, *Mat. Sci. Eng. A* **254**, 282 (1998).
42. J. Liu, D. Jiao, and C. Luo, *Mat. Sci. Eng. A* **527**, 2772 (2010).
43. T. Branza, F. Deschaux-Beaume, G. Sierra, and P. Lours, *J. Mater. Process Tech.* **209**, 536 (2009).
44. J.-O. Nillson, P. Kangas, T. Karlsson, and A. Wilson, *Metall. Mater. Trans. A* **31**, 35 (2000).
45. C. A. Danon and C. Servant, *ISIJ Int.* **45**, 903 (2005).
46. N. S. Lim, H. S. Park, S. I. Kim, C. G. Park, *Met. Mater. Int.* **18**, 637 (2012).
47. S. Zhao, X. Xie, G. D. Smith, S. J. Patel, *Mat. Sci. Eng. A* **355**, 96 (2003).
48. M. F. Mcguire, *Stainless Steels for Design Engineers*, pp.72-79, ASM International, Materials Park, Ohio, USA (2008).
49. H. Hanninen, J. Romu, R. Ilora, J. Tervo, and A. Laitinen, *J. Mater. Process Tech.* **117**, 424 (2001).